Correspondence to:
A. S. Lipatov,
alipatov@umbc.edu

Hybrid Kinetic Model of the Interaction Between the Dense Plasma Clouds and Magnetospheric Plasma on Large Time and Spatial Scales, and Comparison With MMS Observations

A. S. Lipatov[1,2] , L. A. Avanov[2,3] , and B. L. Giles[2]

[1]University of Maryland Baltimore County, Baltimore, MD, USA, [2]NASA Goddard Space Flight Center, Greenbelt, MD, USA, [3]University of Maryland, College Park, MD, USA

Abstract We present a new simulation results of the cloud dynamics in the ambient magnetospheric plasma on the large time and spatial scales. It was assumed that these impulsive structures observed by the MMS spacecraft originally were created because of the reconnection at the magnetopause. Our new 3-D hybrid kinetic modeling on the large time and spatial scales captures several of these processes: an excitation of the electromagnetic waves (whistler and shear-Alfvén waves) and plasma instabilities (mirror and flute); a formation of shock waves, and collapsing diamagnetic cavity; particle acceleration. A strong overshoot in plasma density profile was observed in the modeling and MMS observation at the interface between the cloud and magnetospheric plasma. The cloud expansion into ambient magnetospheric plasma causes the flute waves connected with excitation of the Rayleigh-Taylor instability observed at the overshoot in plasma density profile across the external magnetic field. The modeling demonstrates a formation of the whistler waves at the initial stage which propagate in the external magnetic field direction. At the later stage, a formation of shear-Alfvén waves was observed.

1. Introduction

The plasma processes in the environment of the dense plasma cloud moving in the dayside magnetospheric plasma was studied by a use of unique MMS spacecraft observations and hybrid multiscale modeling on the large spatial and time scales. The results presented will be important for understanding particle acceleration, low-frequency wave excitation and global instability of the plasma configuration during active space plasma experiments, under astrophysical explosions, and plasma systems with reversed magnetic field configuration. The results will be also important for understanding the plasma environment of planetary moon moving through magnetospheric plasma (e.g., Io, Europa, Titan and the Moon).

Extremely dense impulses were observed by MMS spacecraft (Burch et al., 2016) when the spacecraft was located at the dawn-side terminator as shown in Figure 1 (left) from Lipatov et al. (2021). The plasma data are provided by the Fast Plasma Investigation (FPI) (Pollock et al., 2016), while the magnetic field data are produced by the two MMS flux-gate magnetometers (Russell et al., 2016). Figure 1, panels (b–f) shows the plasma data which were received in the burst mode with time resolution 150 ms inside 3 min interval centered at the density peak. There were no significant perturbations in the solar wind observed in the OMNI WIND data (not shown here), however, the interplanetary magnetic field component Bz component was strictly negative that suggests an intensive reconnection at the subsolar magnetopause. The time interval between strong density peaks in panel (a) are about 20–30 min. In previous paper by Lipatov et al. (2021) the same data sets from MMS have been used together with a hybrid simulation to reveal what processes can occur when dense plasma cloud moves in ambient magnetospheric plasma on small time scale.

According to the paper by Akhavan-Tafti et al. (2018) these impulsive structures can be created by moving flux transfer events (FTE's) or by magnetic reconnection inside the magnetopause current layer, or by mirror wave instabilities inside the low latitude boundary layer. They estimated the size, core magnetic field strength and magnetic flux content, and concluded that spacecraft trajectory most likely passed through these structures. Statistical analysis gives the following mean diameter of these impulsive structures $1,700 \pm 400$ km. The average magnetic flux content is of 100 ± 30 kWb. However, the source and formation of these clouds within the magnetopause is out of scope of our paper.
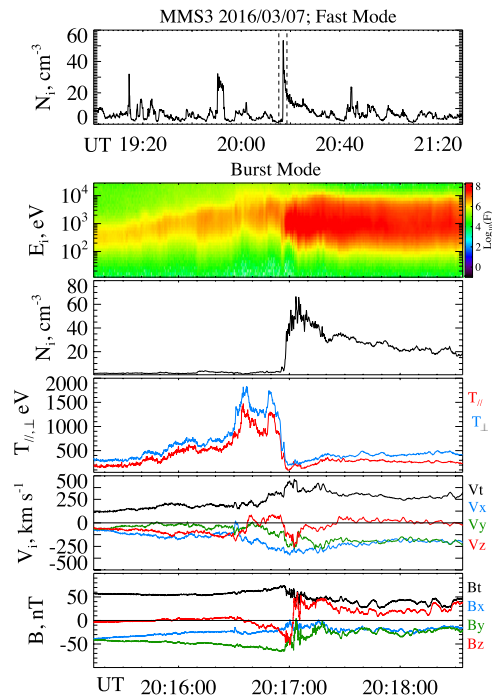
Figure 1. Profiles of the impulsive structures captured by the MMS spacecraft (MMS3 data). The upper panel (a) shows the plasma density recorded in Fast Survey mode with 4.5 s time resolution. Two dashed lines bound a time interval for The particular pulse (between two dashed lines) recorded in a burst mode with time resolution 150 ms was chosen for modeling study. The other panels show variation of ion energy flux (b), number density (c), ion ($T_{parallel}$ and T_{perp}) temperatures (d), velocity components (e), and magnetic field components (f).

The AMPTE, Starfish and other active plasma experiments (Bernhardt et al., 1987; Dyal, 2006) stimulated a new interest in the study of the processes under interaction between dense plasma cloud and magnetospheric plasmas. Those processes include, an interpenetration of the cloud and ambient plasmas, reflection and acceleration of the upstream ambient ions at the plasma cloud's surface, and excitation of low-frequency waves near the leading edge and within the wake of the cloud.

The study of global macroscopic configuration of expanding plasma cloud within ambient magnetospheric plasmas and excitation of low-frequency instabilities were performed with MHD modeling (Ripin et al., 1987, 1993; Woolsey et al., 2001), however the study of particle acceleration and effects of the non-Maxwellian ion velocity distribution functions (VDF's) requires hybrid kinetic simulations (Antonov et al., 1985; Bashurin et al., 1983; Berezin et al., 1992; Cohen et al., 2019; Golubev et al., 1978; Hewett et al., 2011; Lipatov, 1996, 2002; Lipatov et al., 1994; Winske & Cowee, 2012; Winske & Gary, 2007) and the use of the laboratory installations for a study of these phenomena (e.g., LAPD (UCLA) (Niemann et al., 2013) and KI-1 installation of the Institute of Laser Physics SB RAS, Novosibirsk (Prokopov et al., 2016; Zakharov et al., 2014)). There are basic questions need to be answered concerning the particle heating and acceleration, an excitation of the whistler and Alfvén waves at oblique and quasi-parallel shocks which are formed by the expanding plasma cloud.

Our new modeling of the cloud expansion on the large spatial and time scale demonstrates new features of the ion acceleration, a formation of the overshoot in the cloud density distribution near the interface between cloud and ambient magnetospheric plasma, a formation of the diamagnetic cavity, and the flute wave excitation inside the cloud density overshot across the external magnetic field.

The structure of the paper includes a description of the computational model (Section 2), the analysis of the modeling results and comparison with observations (Section 3), and "Conclusions" section (Section 4).

2. Hybrid Kinetic Model

The study of interaction between the ambient magnetospheric and cloud ions is performed by a use of quasi-neutral hybrid model. The model employs the kinetic (particle) approach for ion dynamics, whereas the fluid approach is used for thr electron dynamics.

The wave-particle interactions on the ion scale ($\rho_{ci} = U_0/\Omega_i$ and $\omega \leq \Omega_i$) are described well for this research. Here, U_0, Ω_i and ρ_{ci} are the bulk velocity of the background plasma, ion frequency and the ion gyroradius.

The ion mass and charge state are $M_1 = M_{H^+}$, $Z_1 = 1$ and $M_2 = M_{H^+}$, $Z_2 = 1$ for magnetospheric and cloud ions. The hybrid model includes the ion motion equation, Ampére's law, induction equation, quasi-neutrality condition, generalized Ohm's law, and an adiabatic approach for the electron pressure (see e.g., Lipatov (2002); Lipatov and Sibeck (2020)).

The leap-frog trapezoid scheme is used for the macro-particle pushing and an implicit integration is used for the electromagnetic equation solution (Lipatov, 2002). This algorithm demonstrated an effective performance in the modeling of the plasma environment near weak comets (Lipatov et al., 2002), the Io (Lipatov & Combi, 2006), the Moon (Lipatov, Cooper et al., 2012; Lipatov, Sittler, et al., 2012; Lipatov, Cooper, Paterson, et al., 2013; Lipatov, Cooper, Sittler, et al., 2013; Lipatov et al., 2018), Europa (Lipatov et al., 2010; Lipatov, Cooper, Paterson, et al., 2013; Lipatov, Cooper, Sittler, et al., 2013) and Titan (Lipatov et al., 2011; Lipatov, Cooper et al., 2012; Lipatov, Sittler, et al., 2012);

The following initial conditions are chosen: a homogeneous ambient background plasma flow with bulk velocity $\mathbf{U}_0$; magnetic and electric fields with values $\mathbf{B} = \mathbf{B}_0$ and $\mathbf{E} = -\frac{\mathbf{U}_0 \times \mathbf{B}_0}{c}$. Spacecraft observations in Burst Mode, Figure 1, panels (b–f) are used as upstream parameters for the modeling (20:15:20 UT). The incoming (upstream) magnetospheric ion velocity distribution functions (VDF's) are approximated with Maxwellian distributions with GSE bulk velocity $U = (-83, -83, -55)$ km/s, thermal ion and electron velocities of 100 km/s and 2,200 km/s, respectively. The value of the plasma density is 2.4 cm^{-3}. The incoming magnetic field has a value $B = (-39.0, 0, -40.0)$ nT. The value of plasma betas and the Alfvén speed are $\beta_i = 0.0125$, $\beta_e = 0.0024$, and $V_A = 780$ km/s. The initial value of the cloud speed in GSE is chosen: $U = (-305, -256, -139)$ km/s; $V_{th,i} = 120$ km/s; $V_{th,e} = 2,400$ km/s. We investigated various initial distributions of the cloud density. The case with the best agreement with observations is presented here. The Gaussian distribution with standard deviation $\sigma = 0.44 \, R_E = 440$ km was used for approximation of the initial profile of the cloud density profile. The peak of the distribution is chosen as $N_{max} \approx 2.8 \times 10^3$ cm^{-3} which exceeds one ($N_{max} \approx 1.4 \times 10^3$ cm^{-3}) used in Lipatov et al. (2021). The value of the effective radius of the Earth $R_E = 1,000$ km reduces the cell size to 8.9 km which is twice smaller than one used in Lipatov et al. (2021) with $R_E = 2,000$ km. That way provides much better numerical resolution of the fine plasma and wave structures. The initial radius of the cloud is also twice smaller than one (880 km) used in Lipatov et al. (2021).

A variable mass of macro-particles allows to reduce the numerical "shot" noise in the cloud density and velocity profiles (Lipatov, 2012). The data from MMS3 are used in the modeling. Due to the small spacecraft separation (<15 km) the data from the other MMS spacecraft are approximately the same on the spatial scale of the processes studied here.

In the modeling X axis is directed along the external magnetic field outward to the magnetopause. The Y axis is perpendicular to the X axis and it coplanar with the X axis and the magnetospheric plasma's bulk velocity. The Z axis direction completes the right-handed coordinate system. The initial location of the cloud center are the following: $x = 0 \, R_E$, $y = 0 \, R_E$ and $z = 0 \, R_E$. In our modeling we superimposed cloud ions on the background plasma. Initially the cloud ions have no radial speed and the cloud expansion is driven by a strong gradient in the cloud density at the interface. A cloud expansion produces a depletion in the background density and the cloud-background system forms a self-consistent interface very fast.

The background ions are injected continuously on the left-handed boundary of the computational domain to support a homogeneous background. The unperturbed ion VDF's and a stationary electromagnetic field are used at the flank boundaries. The cloud and background ions have been removed from computation if they intersect the boundary of the computational domain. The magnetic field was allowed to propagate across the back boundary by the use of the "Sommerfeld" radiation condition (Schot, 1992).

The following dimensions of the computational domain are used in the modeling: ($DX = 10 \, R_E$, $DY = 10 \, R_E$, $DZ = 10 \, R_E$) and ($DX = 18 \, R_E$, $DY = 20 \, R_E$, $DZ = 20 \, R_E$). Here, $R_E = 1,000$ km denotes the effective Earth's radius. The grid points of $1,121 \times 321 \times 321$ and $1,121 \times 501 \times 501$ cover the computational domain. The cloud and magnetospheric ion VDF's are calculated with the particle-in-cell algorithm. This approach provides a good numerical resolution with ≈ 50 and $\approx 80–200$ macro-particle per cell for the cloud and magnetospheric ions. The following time steps $\Delta t_p \le \min(\Delta x, \Delta y, \Delta z)/(16 v_{max})$ and $\Delta t_{EB} = \Delta t_p/16$ are used for particle and electromagnetic field calculation, where Δx, Δy, Δz are the cell sizes. A small time step provides a good algorithm convergence in modeling of the plasma system with low density.

3. Results

The structure of the transition layer between the cloud and ambient magnetospheric plasma is a key factor for understanding wave-particle interactions which result in particle heating and acceleration, low-frequency wave excitation and propagation, and deformation of the interface between the cloud and ambient magnetospheric plasma due to flute wave instability. Now we discuss the results of the modeling and comparison with MMS observations in details.
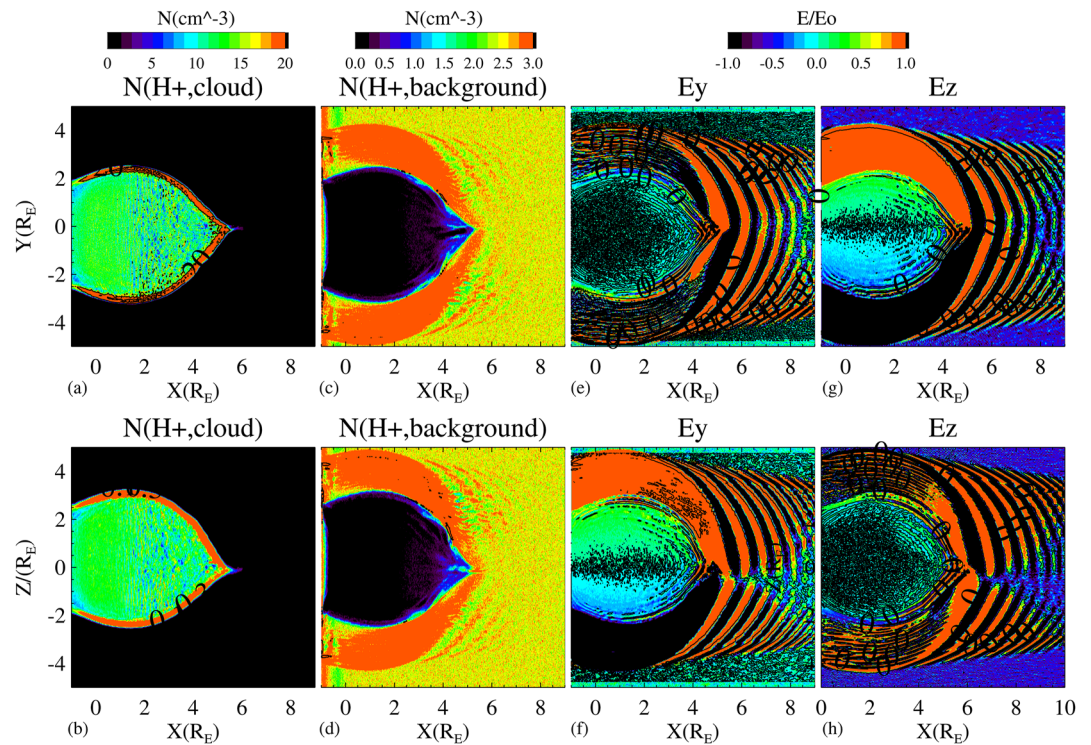
Figure 2. Density profiles of the cloud, magnetospheric plasma and electric field components (E_y, E_z) in $X - Y$ plane (panels (a, c, e, and g), and $X - Z$ plane (panels (b, d, f, and h)) at $t = 2.6$ s. One can see a strong whistler formation. The forward edge of the whistler has a much smaller wavelength than the rear one.

3.1. Global Configuration of the Plasma Cloud Environment

Let consider now the global configuration of the plasma density and electromagnetic field in the cloud environment. Figure 2 panels (a–f) shows 2-D cuts of the density distribution of the cloud ions, magnetospheric ions, and electric field components (E_y and E_z) in $X - Y$ and $X - Z$ planes at time 2.6 s. Dense plasma cloud created a strong overshoot ($N_{overshoot} \approx 15$–17 cm^{-3}) near the interface with the ambient magnetospheric plasma and it serves as piston for a formation of a shock wave which shock transition varies from quasi-parallel/oblique to quasi-perpendicular structures. In the last case there is no a corresponding formation of upstream whistler waves. The plasma cloud–ambient background plasma interaction creates a sharp peak in the density distribution near the lead edge, a strong depletion in the plasma density and a formation of collapsing diamagnetic cavity. A portion of the plasma cloud penetrates deeper into the ambient magnetospheric plasma along the magnetic field (see also Figure 8, panel (d)). One can summarize that the cloud interaction with the ambient magnetospheric plasma results in a formation of the complex plasma structure and wave activity, namely, a formation of both directional strong whistler and shear-Alfvén waves, which propagate along the magnetic field, and the compressional shock-like wave propagating across the magnetic field. The velocity of the center of the cloud has a value of $U \approx (300, -70, -70)$ km/s. Since the spacecraft measurements do not show a whistler formation in the upstream region, one may conclude that the MMS spacecraft trajectory intersected the cloud flank boundary in oblique direction to the X and Y axes.

3.2. Whistler and Alfvén Wave Formation Directed by External Magnetic Field

Let consider the generation of the low-frequency waves at the lead edge directed by the external magnetic field. Figure 3 demonstrates a propagation of the magnetic field perturbations (upper level) and the cloud and ambient density profiles (lower level) along the magnetic field. The modeling shows the formation and propagation of a left-hand polarized whistler wave (as seen from the source point) with transverse magnetic field (B_y and B_z) components upstream of the ambient plasma at later time, (Figure 3, panel (c)). Oscillations in the component B_x are connected with a formation of a compressional mode. The modeling provides the following values for
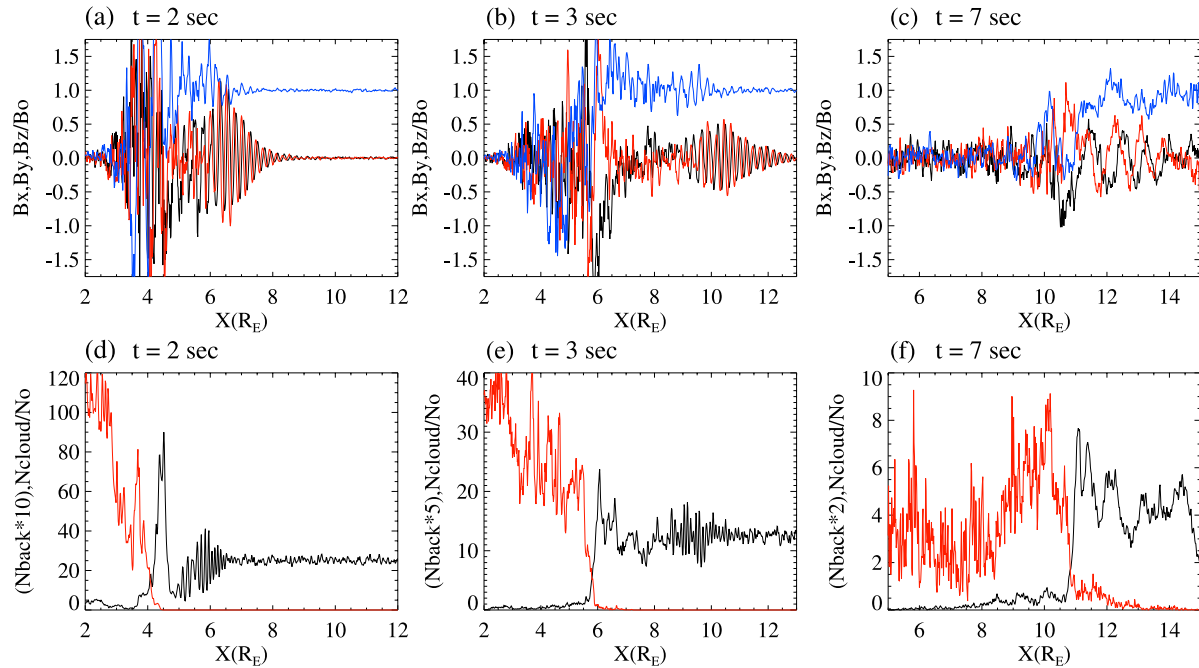
Figure 3. Transition from the whistler to the shear-Alfvén wave formation during the plasma cloud expansion on the large time scale. Top: B_x (blue), B_y (black) and B_z (red) magnetic field perturbations. One can see an attached (a) and detached (b) whistler waves, and a formation of the Alfvén wave (c). Here, $\lambda_{Wh} \approx 100$–220 km; $\lambda_{Aw} \approx 650$–950 km. Bottom: Cloud density (red) and ambient magnetospheric plasma density (black) profiles.

the wavelength, the phase velocity, the frequency, and the amplitude of these oscillations in the rest frame: $\lambda_{Wh} \approx 220$ km, $U_{ph} \approx 1,600$ km/s, $\omega \approx 45$ s^{-1}, and $\delta B \leq 1.0\, B_0$.

Far from the lead edge of the cloud, one can see a significant reduction of the whistler wavelength to the value $\lambda_{Wh} \approx 100.0$ km. At later time, it is expected that the expansion of the plasma cloud will become sub-Alfvénic with the formation of the Alfvénic waves with wavelength of about $\lambda_{AW} \approx 650$–900 km/s. These whistler and Afvénic waves are a similar to the Alfvén wings have been observed near planetary moons and low-frequency waves excited by a pulsed tether in the ionosphere (Chang et al., 1994). At the trailing edge of the plasma cloud, one can see flow deceleration due to expansion of the plasma cloud. Depending on the plasma cloud's initial distribution in the X direction, the back edge may have a smooth profile. Such smooth profiles are observed in the MMS data, see Figure 1 on the right.

The cloud and ambient plasma density profiles had a sharp front with irregular overshoot Fig. 3 (d–f). At an early time oscillations in the ambient plasma profile had a small wavelength ($\lambda \approx 140$ km) upstream the overshoot. At the later time oscillations were about of $\lambda \approx 1,000$ km upstream of the overshoot and its correlated with a compressional part of the whistler and Alfvén waves propagating outside of the interface. Oscillations downstream of overshoot in the ambient plasma ($\lambda \approx 750$ km) were connected with the waves inside the cloud plasma.

The study of the low-frequency wave propagation at far distance from the source may be complicated because of several effects: namely the curvature of the global background magnetic field and nonlinear magnetic field line resonances due to ponderomotive force (Lipatov & Rankin, 2005, 2009 and references therein). The left-handed polarized whistler/Alfvén waves generated by the local sources may be used for killing energetic electrons inside the radiation belts (private communication by Gekelman (2020)). Such type of wave excitation by a transverse magnetic dipole oscillators was considered for example, in Van'yan and Lipatov (1972a, 1972b) and the references therein. The study of the shear-Alfvén wave propagation on the larger distance from the source including above circumstances needs much higher numerical resolution and hence extremely more computational resources and, it is beyound the scope of this paper.
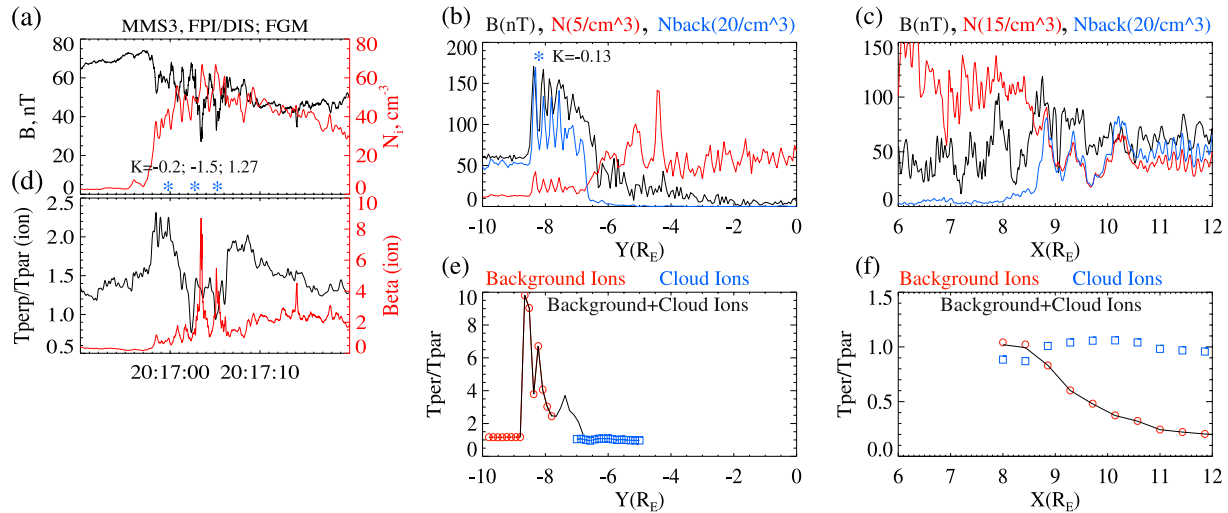
Figure 4. (a): Mirror waves observed by MMS3 spacecraft inside the cloud. (b and c): Total magnetic field (black line), combined density of the cloud and magnetospheric plasma N (red line), and magnetospheric plasma density N_{back} (blue line) profiles along the Y axis (b) and X axis (c) at time $t = 4$ s. The values of total and ambient magnetospheric densities were multiplied by factor 5(15) and 20 correspondingly. (d): Observed the ion temperature anisotropy (black line) and plasma beta (red line). (e and f): The temperature anisotropy of background (red circles) and cloud (blue squares) ions, and the background plus cloud ions (black line). Blue "stars" denote the locations where criterion for the mirror instability (K) was estimated.

3.3. Shock and Mirror Wave Formation at the Flank Edge of the Cloud

Let consider the structure of the shock-like waves formed by the cloud expansion across the external magnetic field.

Figure 4, panel (a) shows MMS observations of the magnetic field (black line) and the plasma density (red line) when the spacecraft moves through the shock-like transition (left). 1-D cuts of the total magnetic field (black line), the ambient magnetospheric plasma density (blue line), and the total plasma density (red line) profiles produced in the modeling are shown in panels (b and c) at the time $t = 4$ s. Across the magnetic field (Y direction), the profile of the plasma cloud density is sharp and the profile of the ambient plasma density show a formation of a quasi-perpendicular shock-like structure without a formation of whistler waves upstream the shock.

Let consider the structure of the mirror waves formed by the cloud expansion.

Figure 4, panel (d) shows the temperature anisotropy in the ion VDF and ion beta observed by MMS spacecraft. Figure 4, panels (e) and (f) demonstrates the ion temperature anisotropy in the background (red circles) and cloud (blue squares) plasma, and the background plus cloud plasma (black line). To identify the mirror instability we use the following criteria for fluid instability condition (see e.g., Chandler et al., 2021; Hasegawa, 1969; Southwood & Kivelson, 1993; Vedenov & Sagdeev, 1958): $K = 1 + \beta_\perp (1 - T_\perp/T_\parallel) < 0$. Our estimation of the value of the parameter K using the temperature anisotropy and beta at the point UT = 20:17:00; 20:17:03 and 20:17:05 gives the following values of K: $K_1 = -0.2$; $K_2 = -1.5$; $K_3 = 1.27$. The above condition for an excitation of the mirror instability is satisfied at two points. However, Equation 7 from Southwood and Kivelson (1993) shows that when the fluid instability condition is not met, the fluid equations predict oscillations. Note that simulated ion temperature anisotropy demonstrates much higher values in Y direction and lower one in X direction.

Mirror mode structures were studied in Chandler et al. (2021). The compressional waves have been also observed in the dawn-side magnetosphere by Korotova et al. (2009) and Rae et al. (2007). They concluded that these waves are connected with the mirror mode instability.

Since the observations do not demonstrate the whistler or Alfvén wave formation in the region outside the cloud, one may conclude that the spacecraft intersected the cloud in the oblique direction to the magnetic field. At the beginning of encounter with the cloud, the spacecraft passed through the oblique shock front and magnetosheath (Figure 1, panels (b) and (c), and the time interval UT 20:15:40–20:16:10) and at the latter time it passed through the magnetosheath of the quasi-perpendicular shock (Figure 1, panel (b) and (c), and the time interval UT 20:16:10–20:16:55).
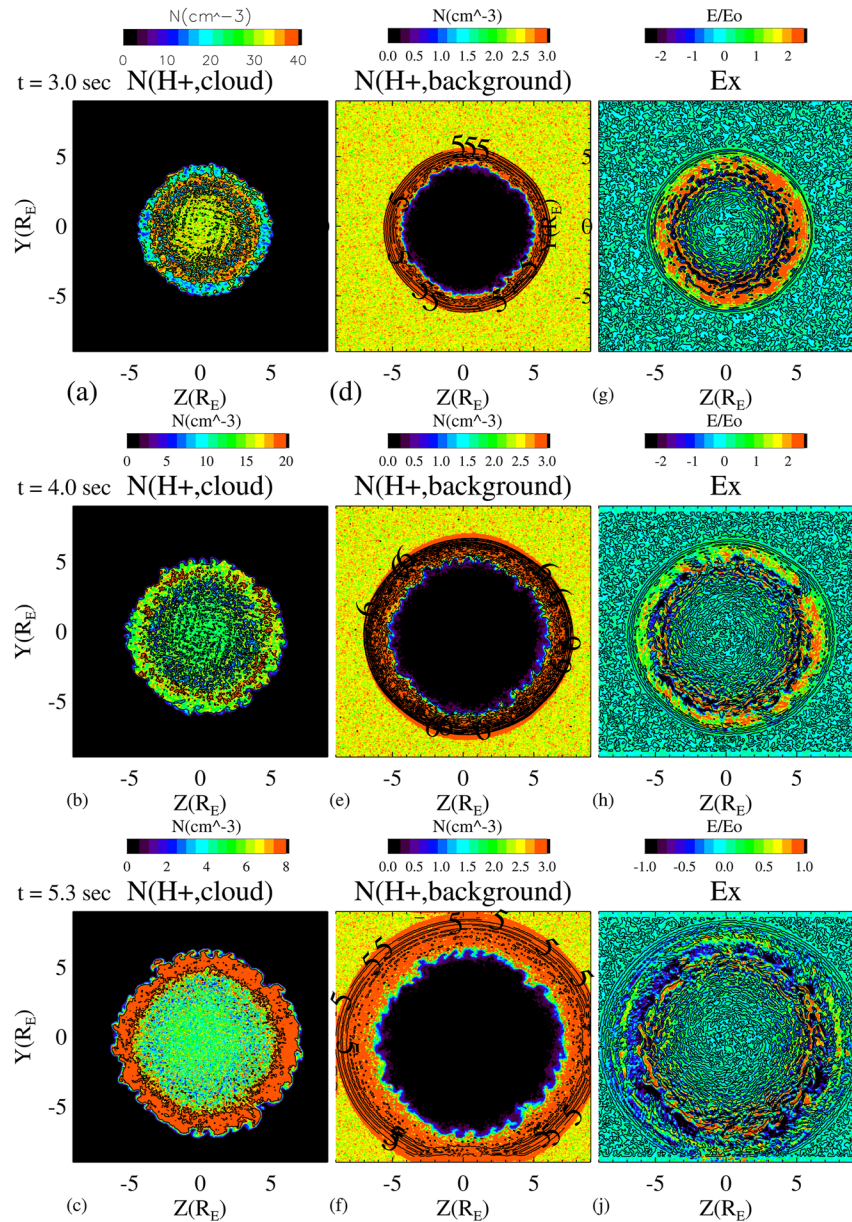
Figure 5. 2-D cuts of the plasma cloud and magnetospheric plasma density, and electric field component E_x profiles in the $Y - Z$ plane. An excitation of the flute-like instability inside the overshoot at the interface between the cloud and magnetospheric plasma. The instability results in to an angular structuring in the interface and it can be modified by effects of the large ion gyroradius in case of heavy cloud ions (e.g., Na^+ in expanding moon's exospheres in the planetary moons). Note that this type of instability was observed in AMPTE experiment.

3.4. Flute Wave Formation Inside the Overshoot in the Density of the Cloud Plasma

Figure 5 demonstrates the time evolution of the cloud and background plasma density, and electric field E_x profiles (2-D cuts) across the magnetospheric magnetic field in the range from $t \approx 2.33$ s to $t \approx 4.01$ s. Figure demonstrates a flute formation connected with an excitation of the Rayleigh-Taylor-like instability inside the overshoot in the plasma density at the later time of an cloud expansion. The wavelength of the perturbations in the overshoot across the magnetic field is about $\lambda_{R-T} \approx (1-2) \times 10^3$ km. At this time the shock front moves with the velocity $V_{front} \approx 1,600$ km/s. The modeling shows the grows of the flutes, however, it not clear a whether this occurs by mode coupling, mode coalescence, or some other non-linear process (Winske, 1988; Winske et al., 2019). The ratio between the values of the Larmor radius estimated with cloud bulk velocity and the density gradient length
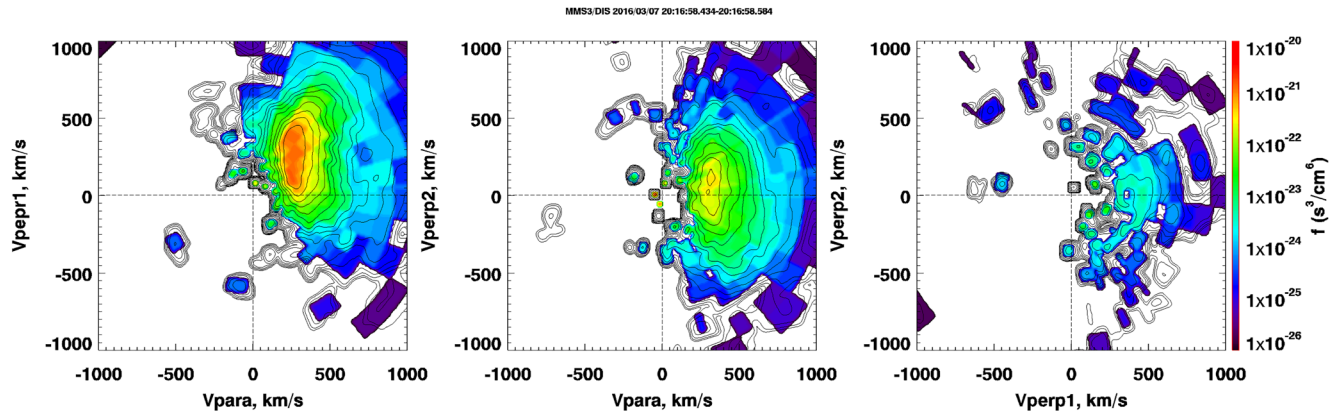
Figure 6. Combined VDF's of the cloud and magnetospheric ions observed by MMS spacecraft near overshoot in the density profile at time 2016/03/07 20:16: 58. U is directed along the external magnetic field, while V and W are directed across the magnetic field.

in our modeling in Figure 5 is about $\rho_{ci}/L \leq 0.7$, where the Larmor radius $\rho_{ci} \approx 120$ km and the thickness of gradient for density profile $L \approx 170$ km.

In case of ($\rho_{ci}/L \approx 1$) the Rayleigh-Taylor instability in the MHD regime will be stabilized (Ripin et al., 1993). During sub-Alfvenic cloud expansion into a magnetospheric plasma the large ion gyroradius ($\rho_{ci}/L > 1$) (e.g., the expanding exosphere of the moon with heaver ions), supports a robust regime of Rayleigh-Taylor instability (see e.g., Huba et al., 1990; Ripin et al., 1993). At this stage flute structures become significant. At later time the cloud expansion will decelerate when the cloud pressure equals the external magnetic field pressure.

The Rayleigh-Taylor instability was also observed in AMPTE (Bernhardt et al., 1987), in CRRES magnetospheric barium releases (Huba et al., 1992), in laser produced plasma experiments (Ripin et al., 1987) and also in plasmas with magnetic confinement (Onishchenko et al., 2011).

A study of the flute-like instability will be also important for understanding astrophysical explosions and the dynamics of the expanding planetary moons exosphere while the moons move in the magnetospheric plasma.

3.5. Acceleration of the Cloud and Ambient Magnetospheric Ions

The cloud expansion into magnetospheric plasma is accompanied by the wave–particle interaction which results in the heating and acceleration of the particles. MMS observations and the modeling demonstrate two distinguish type of the particle accelerations, namely: a particle interaction with shock transition produced by a piston-like cloud expansion; and a beam-beam quasi-parallel interaction directed by external magnetic field.

Figure 6 shows the total ion velocity distribution functions (VDF's) which was observed by MMS spacecraft (MMS3) in the vicinity of the leading edge of the cloud. The VDF includes an anisotropic core which moves along and across magnetic field with velocity $v \approx 250$ km/s and anisotropic halo. The core distribution has a dispersion in velocity of ≈ 250 km/s across (V_{perp1} and V_{perp2}) and ≈ 150 km/s along (V_{para}) the magnetic field. Ion located in the quasi-shell distribution has a velocity of more than 1,000 km/s.

Simulated VDF's of the magnetospheric ions are shown in Figure 7, panels (a–c) at various locations along the X axis. Here, $y = 0.0\ R_E$, $z = 0.0\ R_E$. The position of various columns are shown at the points indicated in panel (d). Here, $U_0 = 100$ km/s. The acceleration of the magnetospheric ions has a value up to $\approx 15\ U_0$ due to cloud expansion with bulk velocity of $10\ U_0$ inside the cavity in the ambient background plasma ($x < 8.7\ R_E$).

Outside the cavity ($x > 9\ R_E$), the VDF's of the ambient ions present a combination of incomplete shell-like distributions with velocity up to $\approx 40\ U_0$ and a relatively cold core (Figure 7, points F5, F6, F12) due to the quasi-parallel beam–beam interactions. The extended cloud expansion provides a much stronger acceleration of the ambient magnetospheric ions ($v \approx 40\ U_0 \approx 4,000$ km/s) than it was observed in an early modeling with a cloud expansion on smaller time and spatial scales (Lipatov et al., 2021).
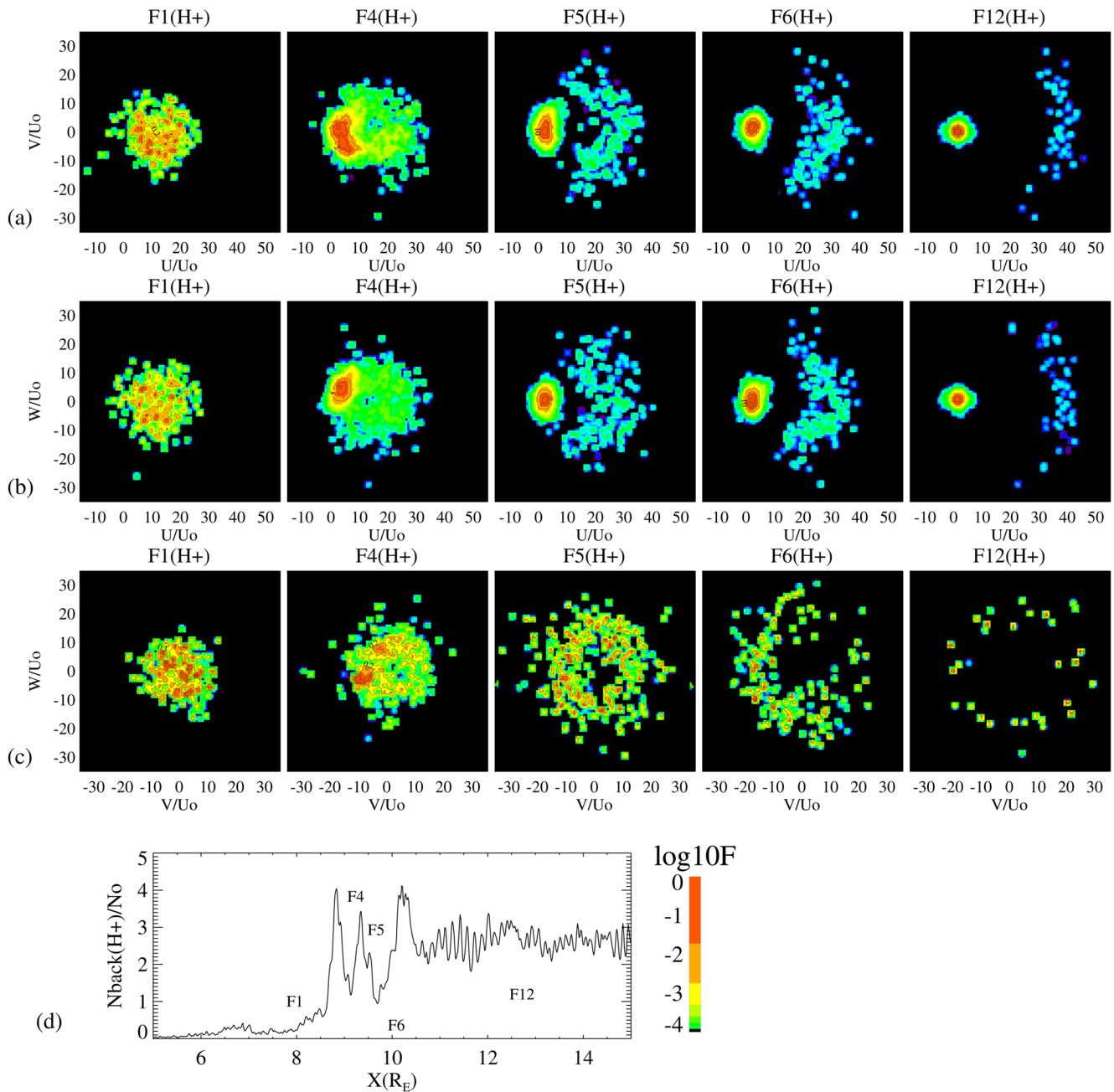
Figure 7. VDFs of the background ions (H^+) (panels (a–c)) along X axis with locations shown with the numbers in the density profile (d). The velocity axes V and U are directed perpendicular to the external magnetic field and W is directed along the external magnetic field. $U_{downstream} = U_0 = 100$ km/s and $t = 4.0$ s.

Figure 8, panels (a–c) shows the VDF of the cloud ions along the X axis. One can see a strong heating and acceleration of the cloud ions with $v \approx (5–10)\ U_0 \approx (500–1,000)$ km/s due to a cloud expansion inside the cloud. The modeling also shows a penetration of the cloud ions into ambient background plasma along the external magnetic field (panel (d)). Outside the cavity in the ambient plasma, the VDF of the cloud ions demonstrate an incomplete quasi-shell distribution with $v \approx (30–35)\ U_0 \approx (3,000–3,500)$ km/s due to the beam-beam instability (Galeev et al., 1987; Gary et al., 1986).

The modeling also demonstrates another type of the ion acceleration due to a formation of the shock structure near the flank of the interface between an expanding cloud and ambient magnetospheric plasmas.
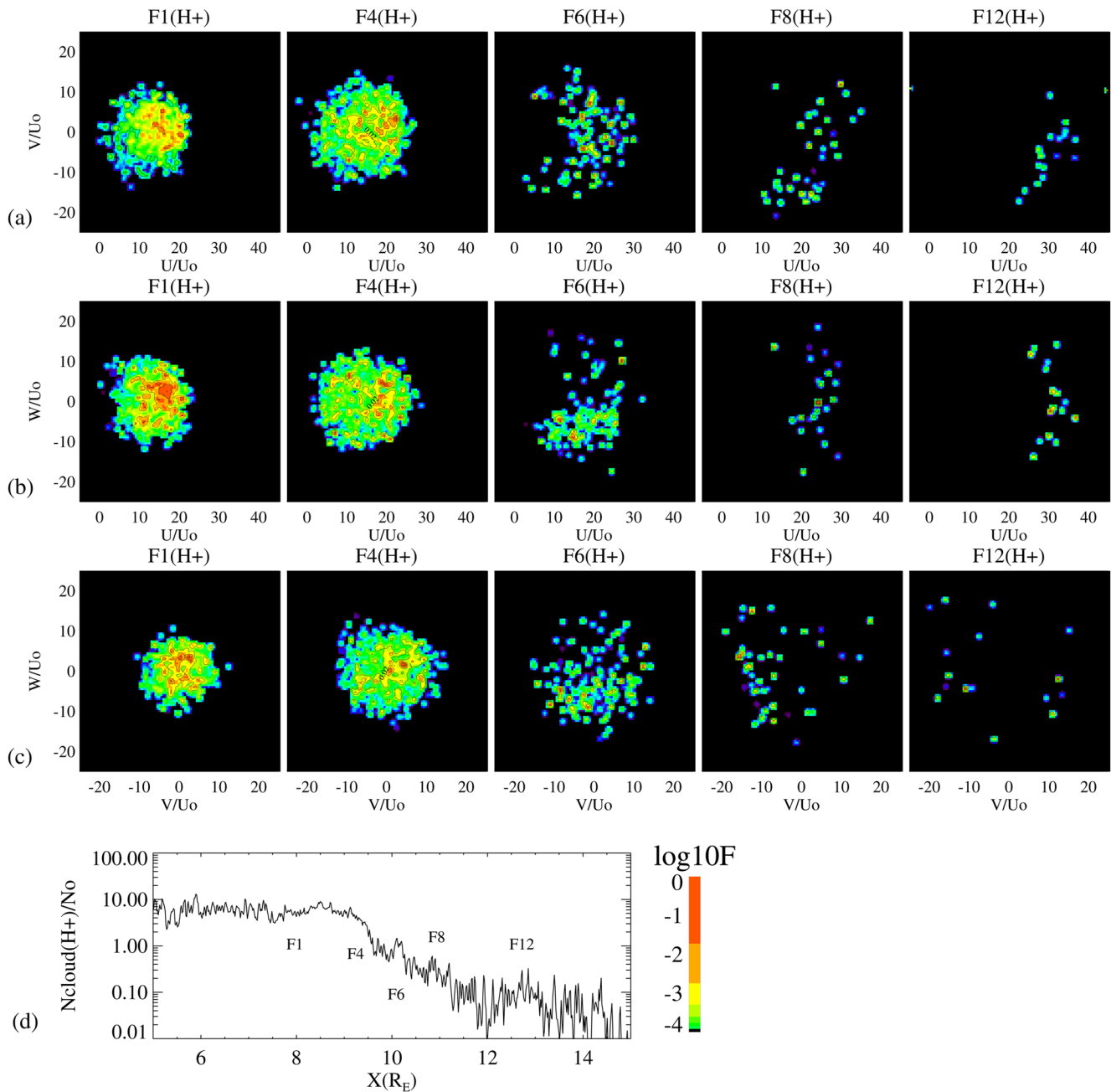
Figure 8. VDFs of the cloud ions (H^+) (panels (a–c)) along X axis with locations shown with the numbers in the density profile (d). The velocity axes V and U are directed perpendicular to the external magnetic field and W is directed along the external magnetic field. $U_{downstream} = U_0 = 100$ km/s and $t = 4.0$ s.

Figure 9, panels (a–c) show VDF's dynamics of ambient magnetospheric ions across the shock transition layer (along the Y axis). The ion VDF corresponds to the relatively cold unperturbed flow upstream of the shock. One can see a gyration of the ambient ions near the shock ramp and the heating of the VDF core while the particles pass the shock transition layer with quasi-perpendicular/oblique structure from point F8 to the point F4.

The VDF of the magnetospheric ions has a strong anisotropy ($T_{i,\perp}/T_{i,\parallel} \approx 10.0$) near the shock-like front. The ion acceleration is not strong as in the case of quasi–parallel interactions, Figure 7. The thin structure of shock-like transition layer is a critical point for particle acceleration. Depending on the wave activity and a formation of a strong ramp one can expect the diffusive particle acceleration and shock surfing acceleration (see, e.g., Drury, 1983; Lipatov & Zank, 1999 and references therein). The observed two peaks in the ion energy plot in
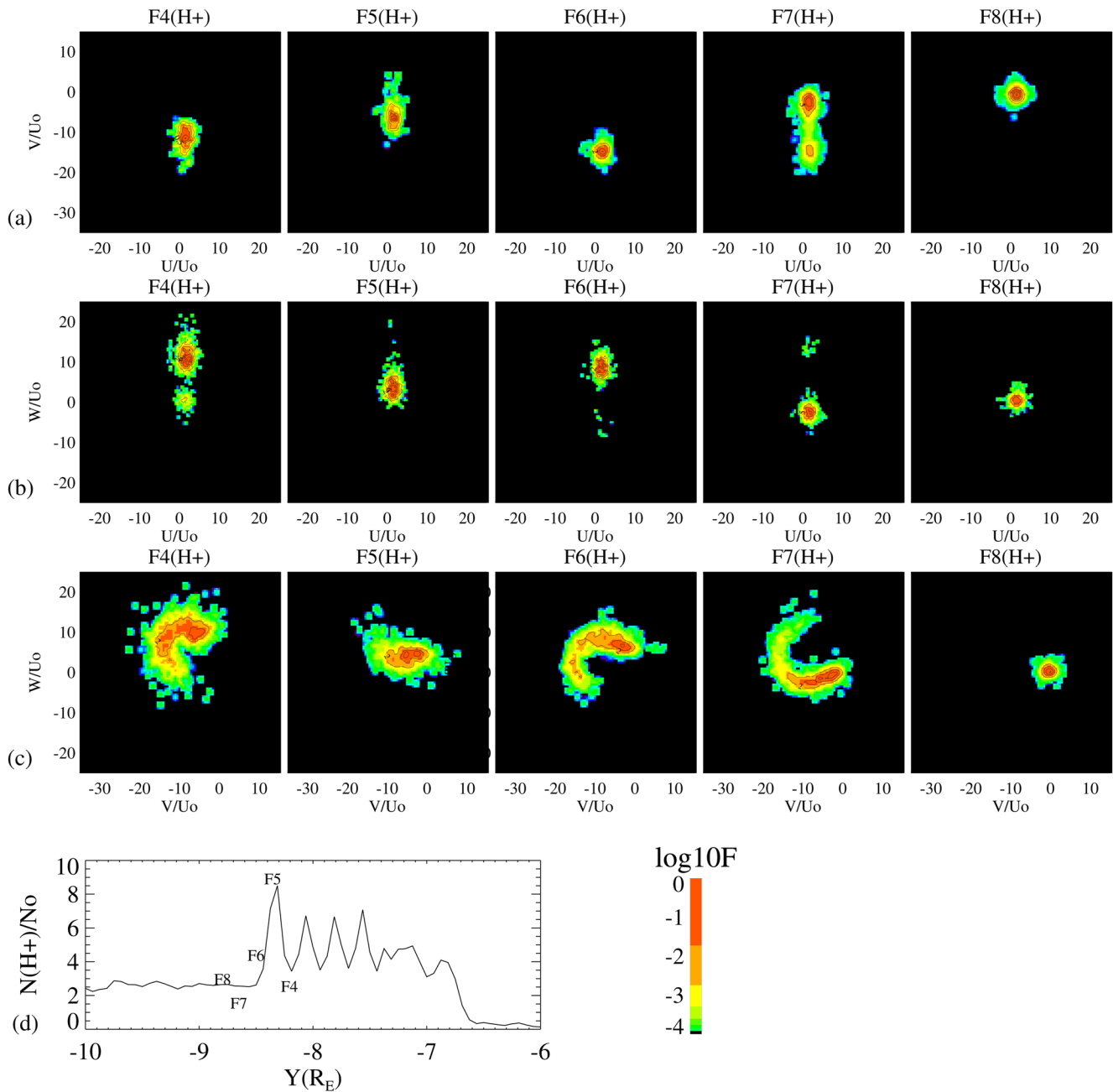
Figure 9. VDFs for the background ions (H^+) (panels (a–c)) along X axis with locations shown with the numbers in the density profile (d). The velocity axes V and U are directed perpendicular to the external magnetic field and W is directed along the external magnetic field. $U_{downstream} = U_0 = 100$ km/s and $t = 4.0$ s.

Figure 1, panel (b) may be produced by the reflecting of foot ion at the ramp of the shock (foot) and the heating downstream ions.

The VDF of the cloud ions along the Y axis is shown in Figure 10, panels (a–c). These VDF's represent a core and quasi-symmetrical halo.

The performed data analysis and the modeling of the ion VDF, density and electromagnetic field conclude that the MMS spacecraft passes through the region with oblique or quasi-parallel interaction structure.
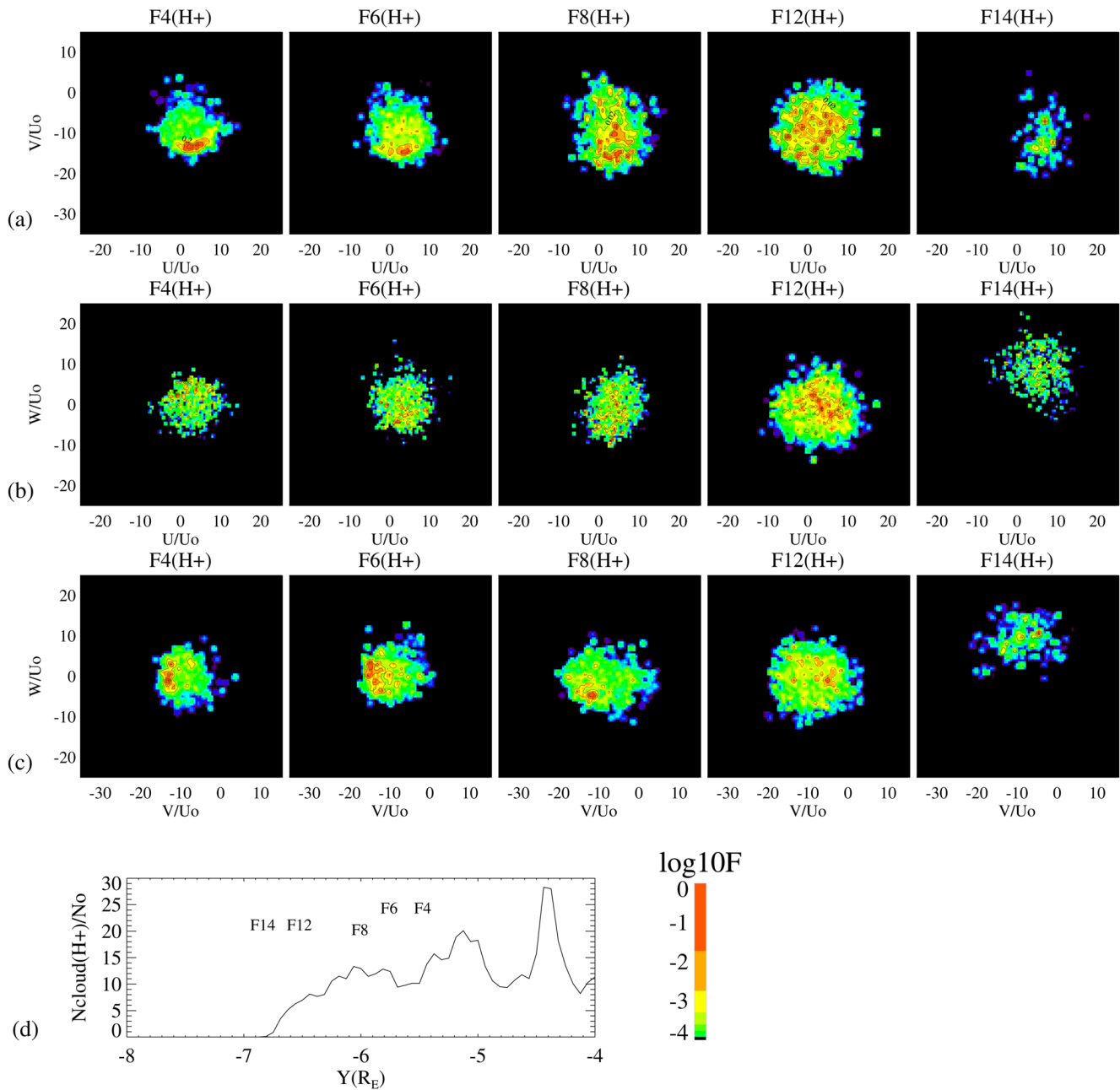
Figure 10. VDFs for the cloud ions (H^+) (panels (a–c)) along X axis with locations shown with the numbers in the density profile (d). The velocity axes V and U are directed perpendicular to the external magnetic field and W is directed along the external magnetic field. $U_{downstream} = U_0 = 100$ km/s and $t = 4.0$ s.

The MMS spacecraft observations provide a good information concerning the Max-wel-lian/quasi-Maxwellian core of the ion VDF, however, the observations cannot provide reliable information about the quasi-shell halo of the VDF of the accelerated ions due to low count rate at higher energies.

4. Conclusions

The high-time-resolution data (150 ms) from the MMS (MMS3) spacecraft together with 3-D hybrid simulation with improved numerical approximation to study, for the first time, the physics of wave–particle interactions triggered by dense plasma cloud moving through the magnetospheric plasma. Results are summarized as follows: (a) The cloud motion generates directional left-hand polarized whistler ($\lambda_{Wh} \approx (100–220)$ km) and shear-Alfvén

($\lambda_{AW} \approx$ (650–900) km) waves while strong compressional waves/shocks are generated across external magnetic field; (b) cloud expansion results in significant ion heating and acceleration. High energy ions with velocity $v > 4,000$ km/s (100 keV) from the shell-like halo of the VDF can damage spacecraft's critical electronic devices; (c) ion temperature anisotropy may generate EMIC and mirror-ballooning waves in the magnetospheric plasma; (d) cloud expansion also results in a formation of collapsing diamagnetic cavity in the cloud-magnetospheric plasma system; and (e) flute waves associated with an excitation of the Rayleigh-Taylor instability were observed in the modeling inside the overshoot in the cloud density across magnetic field. Such waves must be seen at the expanding external boundary of the moon's exosphere in the planetary magnetospheres.

Followup work will focused on the particle shock surfing acceleration (see e.g., Lipatov & Zank, 1999), Fermi particle acceleration and electromagnetic instabilities (mirror, whistler and shear-Alfvén waves) utilizing an effective hybrid modeling algorithms for example, PM-CPK by Lipatov (2012) or EM-SFK by Lipatov et al. (2020, 2022) concepts based on the finite mass method (FMM) by Yserentant (2003) and Gauger et al. (2000), and the Gaussian mixture models (Bishop, 2006; McLachlan & Peel, 2000). The modeling with extremely large computational domain needs a spectral-like numerical resolution that will allow to study of the diamagnetic cavity dynamics at the stage of deceleration in the cloud expansion and the final stage of the cavity collapse.

Data Availability Statement

References

Akhavan-Tafti, M., Slavin, J. A., Le, G., Eastwood, J. P., Strangeway, R. J., Russell, C. T., et al. (2018). MMS examination of FTEs at the Earth's subsolar magnetopause. *Journal of Geophysical Research: Space Physics*, *123*(2), 1224–1241. https://doi.org/10.1002/2017ja024681

Antonov, V. M., Bashurin, V. P., Golubev, A. I., Zhmailo, V. A., Zakharov, Y. P., Orishich, A. M., et al. (1985). A study of the collisionless interpenetrating interaction of super-alfven plasma flows. *Journal of Applied Mechanics and Technical Physics*, *26*(6), 757–763. https://doi.org/10.1007/bf00919519

Bashurin, V. P., Golubev, A. I., & Terekhin, V. A. (1983). The collisionless deceleration of an ionized cloud dispersing in a uniform plasma in a magnetic field. *Journal of Applied Mechanics and Technical Physics*, *24*(5), 614–620. https://doi.org/10.1007/bf00905870

Berezin, Y. A., Vshivkov, V. A., Dudnikova, G. I., & Fedoruk, M. P. (1992). Collisionless slowing down of a plasma cloud in a nonuniform magnetized background. *Soviet Journal of Plasma Physics*, *18*(12), 1567.

Bernhardt, P. A., Roussel-Dupre, R., Pongratz, M. B., Haerendel, G., Valenzuela, A., Gurnett, D. A., & Anderson, R. R. (1987). Observations and theory of the AMPTE barium releases. *Journal of Geophysical Research*, *92*, 5777.

Bishop, C. M. (2006). *Pattern Recognition and machine learning. Information science and statistics* (pp. 1–695). Springer.

Burch, J. L., Moore, T. E., Torbert, R. B., & Giles, B. L. (2016). Magnetospheric multiscale overview and science objectives. *Space Science Reviews*, *199*(1–4), 5–21. https://doi.org/10.1007/s11214-015-0164-9

Chandler, M. O., Schwartz, S. J., Avanov, L. A., Coffey, V. N., Giles, B. L., Moore, T. E., et al. (2021). Observations of mirror mode structures in the dawn-side magnetosphere. *Journal of Geophysical Research: Space Physics*, *126*(2), e2020JA028649. https://doi.org/10.1029/2020JA028649

Chang, C. L., Lipatov, A. S., Drobot, A. T., Papadopoulos, K., & Satya-Narayana, P. (1994). Hybrid simulation of whistler waves generation and current closure by a pulsed tether in the ionosphere. *Geophysical Research Letters*, *21*(11), 1015–1018. https://doi.org/10.1029/94gl00700

Cohen, B. I., Larson, D. J., Belyaev, M. A., & Thomas, V. A. (2019). Topanga: A modern code for E3 simulations. In *2019 IEEE pulsed power and plasma physics orlando, FL*.

Drury, L. O. 'C. (1983). An introduction to the theory of diffusive shock acceleration of energetic particles in tenuous plasmas. *Reports on Progress in Physics*, *46*(8), 973–1027. https://doi.org/10.1088/0034-4885/46/8/002

Dyal, P. (2006). Particle and field measurements of the Starfish diamagnetic cavity. *Journal of Geophysical Research*, *111*(A12), A12211. https://doi.org/10.1029/2006ja011827

Galeev, A. A., Lipatov, A. S., & Sagdeev, R. Z. (1987). Two-dimensional numerical simulation of the relaxation of cometary ions and MHD turbulence in the flow of the solar wind around a cometary atmosphere. *Soviet Journal of Plasma Physics*, *13*(5), 323.

Gary, S. P., Hinata, S., Madland, C., & Winske, D. (1986). The development of shell-like distributions from newborn cometary ions. *Geophysical Research Letters*, *13*(13), 1364–1367. https://doi.org/10.1029/gl013i013p01364

Gauger, C., Leinen, P., & Yserentant, H. (2000). The finite mass method. *SIAM Journal on Numerical Analysis*, *37*(6), 1768–1799. https://doi.org/10.1137/s0036142999352564

Gekelman, W. (2020). *HPD seminar*. NASA GSFC.

Golubev, A. I., Solov'ev, A. A., & Terekhin, V. A. (1978). Collisionless expansion of an ionized cloud in a homogeneous magnetized plasma. *Journal of Applied Mechanics and Technical Physics*, *19*(5), 602–609. https://doi.org/10.1007/bf00850600

Hasegawa, A. (1969). Drift mirror instability of the magnetosphere. *Physics of Fluids*, *12*, 2642–2650. https://doi.org/10.1063/1.1692407

Hewett, D. W., Brecht, S. H., & Larson, D. J. (2011). The physics of ion decoupling in magnetized plasma expansions. *Journal of Geophysical Research*, *116*(A11), A11310. https://doi.org/10.1029/2011ja016904

Huba, J. D., Bernhardt, P. A., & Lyon, J. D. (1992). Preliminary study of the CRRES magnetospheric barium releases. *Journal of Geophysical Research*, *97*(A1), 11. https://doi.org/10.1029/91ja02144

Huba, J. D., Hassam, A. B., & Winske, D. (1990). Stability of sub-Alfvénic plasma expansions. *Physics of Fluids B*, *2*(7), 1676–1697. https://doi.org/10.1063/1.859441

Korotova, G. I., Sibeck, D. G., Kondratovich, V., Angelopoulos, V., & Constantinescu, O. D. (2009). Themis observations of compressional pulsations in the dawn-side magnetosphere, a case study. *Annals of Geophysics*, *27*(10), 1–11. https://doi.org/10.5194/angeo-27-3725-2009

Lipatov, A. S. (1996). 3-D and 2.5-D hybrid multiscale simulation technology: Application to study of forced nonstationary processes at tangential discontinuities. *STEP SIMPO Newletter*, *5*(16), 11–15.

Lipatov, A. S. (2002). *The hybrid multiscale simulation technology. An introduction with application to astrophysical and laboratory plasmas*. Scientific Computation (pp. 1–403). Springer-Verlag. Retrieved from www.Springer.com

Lipatov, A. S. (2012). Merging for particle-mesh complex particle kinetic modeling of the multiple plasma beams. *Journal of Computational Physics*, *231*(8), 3101–3118. https://doi.org/10.1016/j.jcp.2011.12.020

Lipatov, A. S., Avanov, L. A., & Giles, B. L. (2021). Particle acceleration by dense impulsive structures moving in ambient magnetospheric plasma. 3-D hybrid kinetic modeling and MMS observations. *Geophysical Research Letters*, *48*(3), e2020GL088590. https://doi.org/10.1029/2020GL088590

Lipatov, A. S., & Combi, M. R. (2006). Effects of kinetic processes in shaping Io's global plasma environment: A 3D hybrid model. *Icarus*, *180*(2), 412–427. https://doi.org/10.1016/j.icarus.2005.08.012

Lipatov, A. S., Cooper, J. F., Paterson, W. R., Sittler, E. C., Hartle, R. E., & Simpson, D. G. (2010). Jovian plasma torus interaction with Europa: 3D hybrid kinetic simulation. First results. *Planetary and Space Science*, *58*(13), 1681–1691. https://doi.org/10.1016/j.pss.2010.06.015

Lipatov, A. S., Cooper, J. F., Paterson, W. R., Sittler, E. C., Jr., Hartle, R. E., & Simpson, D. G. (2013). Jovian plasma torus interaction with Europa. Plasma wake structure and effect of inductive magnetic field: 3D hybrid kinetic simulation. *Planetary and Space Science*, *77*, 12–24. https://doi.org/10.1016/j.pss.2013.01.009

Lipatov, A. S., Cooper, J. F., Sittler, E. C., Jr., & Hartle, R. E. (2012). Effects of Na^+ and He^+ pickup ions on the lunar-like plasma environment: 3D hybrid modeling. *Advances in Space Research*, *50*(12), 1583–1591. https://doi.org/10.1016/j.asr.2012.07.009

Lipatov, A. S., Cooper, J. F., Sittler, E. C., Jr., & Hartle, R. E. (2013). The light (H^+, H_{2}^+, He^+) and heavy (Na^+) pickup ion dynamics in the lunar-like plasma environment: 3D hybrid kinetic modeling. *Advances in Space Research*, *52*(2013), 1929–1938. https://doi.org/10.1016/j.asr.2013.08.023

Lipatov, A. S., Halekas, J., Sarantos, M., & Cooper, J. F. (2022). *Plasma environment in magnetotail lobe conditions. First results from 3-D hybrid kinetic modeling and comparison with ARTEMIS observation*. ESSOAr. https://doi.org/10.1002/essoar.10510591.1

Lipatov, A. S., Motschmann, U., & Bagdonat, T. (2002). 3D hybrid simulations of the interaction of the solar wind with a weak comet. *Planetary and Space Science*, *50*(4), 403–411. https://doi.org/10.1016/s0032-0633(02)00004-1

Lipatov, A. S., & Rankin, R. (2005). Multi-Fluid and hybrid kinetic modeling of nonlinear field line resonances. In *Meeting of the department of aeronomy and space physics (DASP) of the canadian association of physics*. Crowne Plaza Chateau Lacombe, Edmonton and Athabasca University.

Lipatov, A. S., & Rankin, R. (2009). Nonlinear magnetic field line resonances. Effect of hall term on plasma compression: 1D hall-MHD modeling. *Planetary and Space Science*, *57*(3), 404–414. https://doi.org/10.1016/j.pss.2008.12.012

Lipatov, A. S., Sarantos, M., Cooper, J. F., & Halekas, J. (2020). *Lunar plasma environment in cases with extreme solar wind conditions: First results from 3-D hybrid kinetic modeling and comparison with ARTEMIS observations*. ESSOAR. https://doi.org/10.1002/essoar.10505143.1

Lipatov, A. S., Sarantos, M., Farrell, W. M., & Cooper, J. F. (2018). Effects of multiscale phase-mixing and interior conductance in the lunar-like pickup ion plasma wake. First results from 3-D hybrid kinetic modeling. In M. Horayi & A. Stern (Eds.), *Dust, atmosphere, and plasma environment of the moon and small bodies* (Vol. 156, pp. 117–129). https://doi.org/10.1016/j.pss.2018.02.017

Lipatov, A. S., Sharma, A. S., & Papadopoulos, K. (1994). *Two-dimensional hybrid simulation of whistler and Alfvén wave generated by plasma beams in tangential discontinuities*. University of Maryland Department of Astronomy Report.

Lipatov, A. S., & Sibeck, D. G. (2020). Concerning the interaction of a transmitted interplanetary impulse with a plasmaspheric drainage plume: First results from 3-D hybrid kinetic modeling. *Planetary and Space Science*, *194*, 105104. https://doi.org/10.1016/j.pss.2020.105104

Lipatov, A. S., Sittler, E. C., Jr., Hartle, R. E., Cooper, J. F., & Simpson, D. G. (2011). Background and pickup ion velocity distribution dynamics in Titan's plasma environment: 3D hybrid simulation and comparison with CAPS T9 observations. *Advances in Space Research*, *48*(6), 1114–1125. https://doi.org/10.1016/j.asr.2011.05.026

Lipatov, A. S., Sittler, E. C., Jr., Hartle, R. E., Cooper, J. F., & Simpson, D. G. (2012). Saturn's magnetosphere interaction with Titan for T9 encounter: 3D hybrid modeling and comparison with CAPS observations. *Planetary and Space Science*, *61*(1), 66–78. https://doi.org/10.1016/j.pss.2011.08.017

Lipatov, A. S., & Zank, G. P. (1999). Pickup ion acceleration at low-β_p perpendicular shocks. *Physical Review Letters*, *82*(18), 3609–3612. https://doi.org/10.1103/physrevlett.82.3609

McLachlan, G., & Peel, D. (2000). Finite mixture models. In *Wiley series in probability and statistics* (pp. 1–419). John Wiley.

Niemann, C., Gekelman, W., Constantin, C. G., Everson, E. T., Schaeffer, D. B., Clark, S. E., et al. (2013). Dynamics of exploding plasmas in a large magnetized plasma. *Physics of Plasmas*, *20*(1), 012108. https://doi.org/10.1063/1.4773911

Onishchenko, O. G., Pokhotelov, O. A., Stenflo, L., & Shukla, P. K. (2011). The magnetic Rayleigh–Taylor instability and flute waves at the ion Larmor radius scales. *Physics of Plasmas*, *18*(2), 022106. https://doi.org/10.1063/1.3554661

Pollock, C., Moore, T., Jacques, A., Burch, J., Gliese, U., Saito, Y., et al. (2016). Fast plasma investigation for magnetospheric multiscale. *Space Science Reviews*, *199*(1), 331–406. https://doi.org/10.1007/s11214-016-0245-4

Prokopov, P. A., Zakharov, Y. P., Tishchenko, V. N., Shaikhislamov, I. F., Boyarintsev, E. L., Melekhov, A. V., et al. (2016). Laser plasma simulations of the generation processes of Alfven and collisionless shock waves in space plasma. *Journal of Physics: Conference Series*, *769*, 012086. https://doi.org/10.1088/1742-6596/769/1/012086

Rae, I. J., Mann, I. R., Watt, C. E. J., Kistler, L. M., & Baumjohann, W. (2007). Equator-S observations of drift mirror mode waves in the dawnside magnetosphere. *Journal of Geophysical Research*, *112*(A11), A11203. https://doi.org/10.1029/2006JA012064

Ripin, B. H., Huba, J. D., McLean, E. A., Manka, C. K., Peyser, T., Burris, H. R., & Grun, J. (1993). SubAlfvénic plasma expansion. *Physics of Fluids B: Plasma Physics*, *5*(10), 3491–3506. https://doi.org/10.1063/1.860825

Ripin, B. H. E., McLean, E. A., Manka, C. K., Pawley, C., Stamper, J. A., Peyser, T. A., et al. (1987). Large radius interchange instability. *Physical Review Letters*, *59*(20), 2299–2302. https://doi.org/10.1103/PhysRevLett.59.2299

Russell, C. T., Anderson, B. J., Baumjohann, W., Bromund, K., Dearborn, D., Fischer, D., et al. (2016). The magnetospheric multiscale magnetometers. *Space Science Reviews*, *199*(1), 189–256. https://doi.org/10.1007/s11214-014-0057-3

Schot, S. H. (1992). Eighty years of Sommerfeld's radiation condition. *Historia Mathematica*, *19*(4), 385–401. https://doi.org/10.1016/0315-0860(92)90004-u

Southwood, D., & Kivelson, M. G. (1993). Mirror instability: 1. Physical mechanism of linear instability. *Journal of Geophysical Research*, *98*(A6), 9181–9197. https://doi.org/10.1029/92ja02837

Van'yan, L. L., & Lipatov, A. S. (1972a). Some characteristics of magnetic dipole emission in a plasma with finite conductivity. *Geomagnetism and Aeronomy*, *12*, 319.

Van'yan, L. L., & Lipatov, A. S. (1972b). Three-dimensional hydromagnetic disturbances generated by a magnetic dipole in an anisotropic plasma. *Geomagnetism and Aeronomy*, *12*, 316.

Vedenov, A. A., & Sagdeev, R. Z. (1958). Some properties of plasma with an anisotropic ion velocity distribution in a magnetic field. In M. A. Leontovich (Ed.), *Plasma physics and the problem of controlled thermonuclear reactions* (Vol. 3, pp. 332–339). Pergamon.

Winske, D. (1988). Short-wavelength modes on expanding plasma clouds. *Journal of Geophysical Research*, *93*(A4), 2539. https://doi.org/10.1029/ja093ia04p02539

Winske, D., & Cowee, M. (2012). *Conditions for debris-background ion interactions and collisionless shock wave generation* Report LA-UR-12-22823. Los Alamos National Lab. (LANL). https://doi.org/10.2172/1045984

Winske, D., & Gary, S. P. (2007). Hybrid simulations of debris–ambient ion interactions in astrophysical explosions. *Journal of Geophysical Research*, *112*(A10), A10303. https://doi.org/10.1029/2007JA012276

Winske, D., Huba, J. D., Niemann, C., & Le, A. (2019). Recalling and updating research on diamagnetic cavities: Experiments, theory, simulations. *Frontiers in Astronomy and Space Sciences*, *5*(51), 1–14. https://doi.org/10.3389/fspas.2018.00051

Woolsey, N. C., Abou Ali, Y., Evans, R. G., Grundy, R. A. D., Pestehe, S. J., Carolan, P. G., et al. (2001). Collisionless shock and supernova simulations on VULCAN. *Physics of Plasmas*, *8*(5), 2439–2445. https://doi.org/10.1063/1.1351831

Yserentant, H. (2003). The convergence of the finite mass method for flows in given force and velocity fields. In M. Griebel & M. A. Schweitzer (Eds.), *Meshfree methods for partial differential equations*, *Lecture notes in computational science and engineering* (Vol. 26, pp. 419–440). Springer. https://doi.org/10.1007/978-3-642-56103-0_29

Zakharov, Y. P., Ponomarenko, A. G., Terekhin, V. A., Antonov, V. M., Boyarintsev, E. L., Melekhov, A. V., et al. (2014). Generation of collisionless shocks by laser-plasma piston in magnetized background: Experiment "BUW". *Plasma Physics and Technology*, *1*(3), 163–165.